optica

# Multi-slice ptychography with large numerical aperture multilayer Laue lenses

Hande Öztürk,[1] Hanfei Yan,[1] Yan He,[1,2] Mingyuan Ge,[1] Zhihua Dong,[3] Meifeng Lin,[3] Evgeny Nazaretski,[1] Ian K. Robinson,[4,5,6] Yong S. Chu,[1] and Xiaojing Huang[1,*]

[1]National Synchrotron Light Source II, Brookhaven National Laboratory, Upton, New York 11973, USA
[2]Shanghai Synchrotron Radiation Facility, Shanghai Institute of Applied Physics, Shanghai 201204, China
[3]Computational Science Initiative, Brookhaven National Laboratory, Upton, New York 11973, USA
[4]Condensed Matter Physics and Materials Department, Brookhaven National Laboratory, Upton, New York 11973, USA
[5]Research Complex at Harwell, Didcot, Oxfordshire, OX11 0DE, UK
[6]London Centre for Nanotechnology, University College London, London, WC1H 0AH, UK
*Corresponding author: xjhuang@bnl.gov

Received 3 January 2018; revised 19 March 2018; accepted 25 March 2018 (Doc. ID 318977); published 9 May 2018

**The highly convergent x-ray beam focused by multilayer Laue lenses with large numerical apertures is used as a three-dimensional (3D) probe to image layered structures with an axial separation larger than the depth of focus. Instead of collecting weakly scattered high-spatial-frequency signals, the depth-resolving power is provided purely by the intense central cone diverged from the focused beam. Using the multi-slice ptychography method combined with the on-the-fly scan scheme, two layers of nanoparticles separated by 10 μm are successfully reconstructed with 8.1 nm lateral resolution and with a dwell time as low as 0.05 s per scan point. This approach obtains high-resolution images with extended depth of field, which paves the way for multi-slice ptychography as a high throughput technique for high-resolution 3D imaging of thick samples.** 

***OCIS codes:*** (110.7440) X-ray imaging; (100.5070) Phase retrieval; (340.0340) X-ray optics.

https://doi.org/10.1364/OPTICA.5.000601

## 1. INTRODUCTION

The continuous advancements in x-ray sources, optics, detectors, and algorithms have significantly improved the achievable spatial resolution of x-ray microscopy. Coherent diffraction imaging (CDI) [1,2] and its scanning version ptychography [3,4] emerged as a promising approach for reaching diffraction limited resolution in both 2D [5,6] and 3D [7,8]. Although it is well recognized that this diffraction-based imaging technique is able to resolve features beyond the resolution limit imposed by x-ray optics, it has been pointed out that using a nano-focused beam for ptychography provides several benefits [9], including reducing the number of necessary detector pixels, relaxing x-ray bandwidth, ameliorating detection dynamic range, enabling high-resolution multi-modality imaging mode, and decreasing the required dwell time. In the hard x-ray regime, the multilayer Laue lens (MLL) has been proposed as a volume diffractive optics alternative to Fresnel zone plate to produce sub-10 nm focus with high efficiency [10,11]. Since its first demonstration [12], the achieved focus size has been steadily improved to sub-10 nm scale with flat or wedged MLLs [13–19]. Integrating scanning probe microscopy with ptychography gains accumulating popularity for its multi-modality imaging capability with high spatial resolution [20–22]. The throughput of this approach was further enhanced by operating in the on-the-fly scan mode [23–26].

On the same journey to achieve smaller focal size and higher spatial resolution, intrinsic physics principles rigorously enforce that the depth of focus (DoF) from optics or depth of field from detection shrinks consistently with the decrement of the desired resolution. With thick samples, the propagation of the illumination wavefront inside the sample becomes non-negligible, or the multiple-scattering effect starts to make impact, either of which breaks the validity of the projection approximation. Thus, the DoF limits the sample thickness for achieving diffraction-limited resolution [27]. A recent development in ptychography method alleviates the DoF limitation by adopting the multi-slice concept [28,29] and decomposing the thick sample into a series of thin slices, where the scattering on each slice satisfies the projection approximation [30]. The multi-slice ptychography approach includes multiple scattering into the reconstruction engine, and recovers several axial planes simultaneously. 3D structures were obtained using this method with visible light [31] and electron [32] microscopy. In the visible light regime, tilting the incident beam in a manner of Fourier ptychography [33] has been demonstrated to be able to assist plane separation [34], and the multi-slice Fourier ptychography produced high-quality 3D images [35]. Achieving high depth resolution with x-rays is more challenging because of the technical difficulties in fabricating high-numerical-aperture (NA) x-ray lenses. So far, the multi-slice

ptychography demonstrations with x-rays rely on the longitudinal component of the high-spatial-frequency scattering signal on a curved Ewald sphere. As the scattering intensity dramatically drops with spatial frequency [36], collecting weak high-$q$ signal requires 10s of seconds exposure time per scan point [37], or extends the $q$-range of diffraction patterns using the precession method by assembling data collected from a tilting sample [38,39]. The long dwell time per scan point and multiple exposures limit the data acquisition throughput of the multi-slice ptychography method.

High-NA MLLs provide an opportunity to achieve a moderate depth resolution using the intense cone diverged from the focused beam (or the "holographic" region [40]) in the far field, rather than pursuing weakly scattered signal outside the central cone. The DoF of the MLLs used in the experiment is about 4 μm, which is significantly narrower than those of Kirkpatrick–Baez (KB) mirrors (6 mm) [37–39] and the zone plate (72 μm) [27], used in reported multi-slice ptychography measurements. We demonstrate that two layers of nanoparticles separated by 10 μm along the axial direction are successfully reconstructed with a dwell time as low as 0.05 s using the on-the-fly scan mode. This approach is expected to remarkably increase the throughput of the multi-slice ptychography method and provides an alternate path of performing high-resolution 3D visualization for thick specimens or samples within complex *in situ* environments.

## 2. EXPERIMENTAL RESULTS

The experiment was performed at the Hard X-ray Nanoprobe (HXN) beamline, National Synchrotron Light Source II (NSLS-II). X-ray photons at 12 keV filtered by a double crystal Si(111) monochromator were pre-focused at the secondary source aperture (SSA) plane, which is about 15 m in front of the nano-focusing optics. The coherent flux was selected by a 50 × 30 μm SSA opening and illuminated on a pair of MLLs with the same 4 nm outmost zone width and lateral apertures $A$ of 53 μm and 43 μm, respectively. At 12 keV, the focal lengths $f$ of these two lenses are 5.2 mm and 4.2 mm, respectively, and the DoF defined by the NA is $\lambda/(\mathrm{NA})^2 = \lambda(2f/A)^2 = 3.9$ μm. The HXN microscope is designed to conduct high-resolution multi-modal scanning probe measurements using MLLs [41–44]. To create a diffraction-limited point focus, the crossed MLL pair has to be aligned better than the DoF along the longitudinal direction [45] and with an orthogonality better than 0.01° [46]. The experimental setup is illustrated in Fig. 1. The specimen used in the experiment consists of two planes of nanoparticles on two sides of a 10 μm thick silicon wafer. On the front surface, gold nano crystals were prepared by annealing 20 nm thick gold film at 800°C for 8 h. On the rear surface, the suspension solution of micrometer-sized nickel oxide particles was drop-casted and assembled to clusters with various dimensions. The insets in Fig. 1 show the scanning electron microscope (SEM) images of the particles on both surfaces. The diffraction patterns were recorded by a pixelated area detector (Merlin from Quantum Detectors [47]) with 55 μm pitch placed 0.5 m downstream from the sample.

The focused wavefront was measured with a dataset collected with only a gold particle in the field of view, as shown in Supplement 1 Fig. S2. The propagation series of the recovered x-ray probe is shown in Figs. 2(a) and 2(b). At the focal plane, the beam size is 12.5 × 11.8 nm, as shown in Fig. 2(c). The

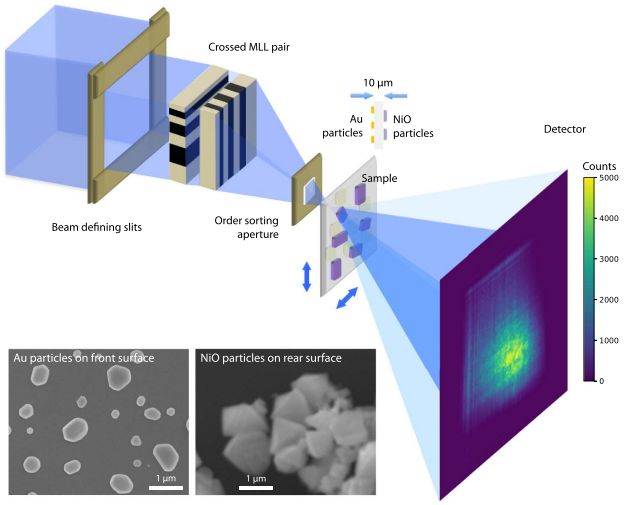


**Fig. 1.** Illustration of the experimental setup for the multi-slice ptychography measurement. Incident 12 keV x-rays are focused by a pair of crossed MLLs and illuminate the sample consisting of two layers of nanoparticles, with the front surface placed 20 μm downstream of the focal plane. The diffraction patterns are collected by a pixelated detector placed 0.5 m from the sample plane. A typical 128 × 128 pixel array with 0.05 s dwell time is shown. The inset SEM pictures show the gold and nickel oxide nanoparticles on the front and rear surfaces, respectively.

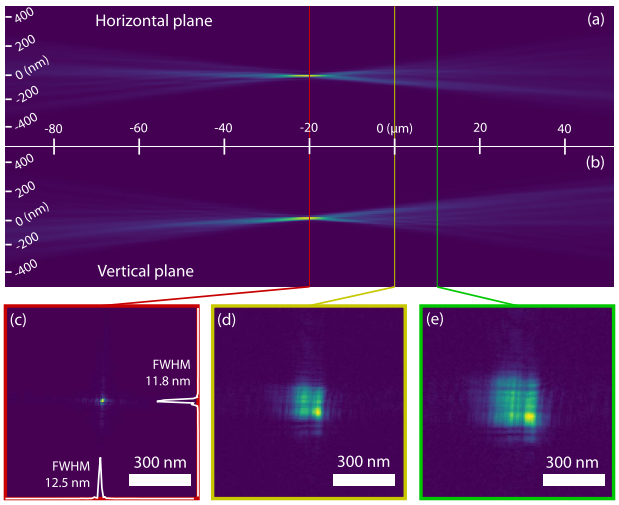


**Fig. 2.** Highly convergent x-ray beam focused by MLLs. (a) and (b) are the propagation series of the focused wavefront. (c) Beam size is 12.5 × 11.8 nm at the focal plane. The undisturbed wavefronts on the front and rear surfaces of the 10 μm thick sample are shown in (d) and (e), respectively.

multi-slice ptychography measurements were conducted at a defocal plane with an enlarged probe size for an improved overlapping condition [48]. The front surface of the sample was placed 20 μm downstream from the focal plane. The undisturbed probe wavefronts on both sides of the 10 μm thick sample are shown in Figs. 2(d) and 2(e), respectively. Two datasets were collected at a sample location with both gold and nickel oxide particles present in the field of view. Dataset 1 covers a 2 × 2 μm area using the step scan scheme following a Fermat spiral

trajectory [49] with a 30 nm average scan step size and 0.5 s exposure time at each position (a typical diffraction pattern is shown in Supplement 1 Fig. S1). This scan pattern eliminates periodic artifacts and optimizes the overlap condition for ptychography. To further increase the measurement throughput, dataset 2 was collected using the on-the-fly scan scheme, and zoomed in a $1.2 \times 1.2$ μm regime using a $60 \times 60$ grid with 20 nm step size and 0.05 s exposure time. The cropped $128 \times 128$ pixel array of a typical diffraction pattern with 0.05 s dwell time is shown on the detector panel in Fig. 1. The scattering intensity concentrates inside the holographic area, reflecting the NA of the MLLs. The holographic area covers about $90 \times 90$ pixels, which provides an estimate of the lens DoF of 4.2 μm and is consistent with the value 3.9 μm calculated using lens parameters. If the scattering signal outside the holographic area can be collected with sufficient signal-to-noise ratio (SNR) and its phase can be faithfully reconstructed, the achievable DoF can go beyond the DoF imposed by the lens. However, we noticed that crossing the boundary of the central cone, the photon counts drop down by 3 orders of magnitude to single counts level. Moving away from the central area, the scattering signal will continuously decrease, roughly inversely proportional to the fourth power of spatial frequency [36]. Collecting high-$q$ scattering signal becomes rather challenging, which requires one or more of the following: strongly scattering and radiation hard specimen, long exposure time, and high dynamic range of detection. These conditions may not always be easily satisfied in practical applications; thus, we explore an alternative approach by using only the signal inside the intense holographic area and relying on the DoF provided by nano-focusing MLL lenses to reach high lateral and moderate depth resolution with high throughput.

The collected datasets were first reconstructed using conventional ptychography with the difference map algorithm [50] assuming structures on one plane. In the CDI reconstruction process, the constraints imposed in real space break the propagation ambiguity and determine the plane where the features are in focus [51,52]. Similarly, the probe wavefront defines the reconstruction plane in ptychography [53]. This effect is clearly seen in Fig. 3. For both datasets, two reconstructions were performed using the probe wavefronts at the front [Fig. 2(d)] and rear [Fig. 2(e)] surfaces, respectively. Figures 3(a) and 3(d) show that the gold particles are in focus and nickel oxide particles are out of focus, when the probe at the front surface was used. The reverse effect is obtained when the probe at the rear surface was used, as shown in Figs. 3(b) and 3(e). Since these two probe functions were numerically generated by propagating the recovered beam at the focal plane with 10 μm distance difference, their ability to bring corresponding planes into focus confirms that the separation between two nanoparticle layers is 10 μm, which also agrees with the SEM measurement (shown in Supplement 1 Fig. S4).

The multi-slice ptychography method was implemented with the difference map algorithm in this experiment. The wavefront at the front surface was used at the initial probe function, and the object functions at two planes were initiated as the square root of the obtained image from conventional ptychography reconstruction [39]. The multi-slice reconstruction took 2000 iterations, during which the probe function was fixed for the first 50 iterations. Figures 4(a) and 4(b) show the recovered phases on the front and rear planes for dataset 1 with the Fermat spiral scan trajectory and 0.5 s dwell time. The gold and nickel oxide particles were well separated and sharply displayed on their corresponding planes. They agree very well with the fluorescence maps, as shown in Figs. 4(e) and 4(f), collected simultaneously with the ptychography measurement. Since the scan followed a non-Cartesian scan pattern, the obtained fluorescence maps were interpolated onto a mesh grid with 30 nm pixel size (also shown in Supplement 1 Fig. S3). Because the measurement was performed at a defocal plane, the fluorescence maps are not as sharp as the ptychography reconstructions. The residual shadows of gold and nickel oxide particles were found on the wrong planes, which mainly resemble the particle shapes. It has been pointed out that these low-spatial-frequency features are very difficult to be axially separated, because they are similar at different planes and require larger separation distance to be decoupled [27,54]. These mixture features are also considered as one of the ambiguity sources for the multi-slice ptychography reconstruction [30]. Despite these residual mixed features, a clean projected image of the scanned region is generated by multiplying two reconstructed slices. Figure 3(c) shows the obtained projection image for dataset 1. Compared with results from conventional reconstructions, features on both surfaces are in focus, which indicates that the

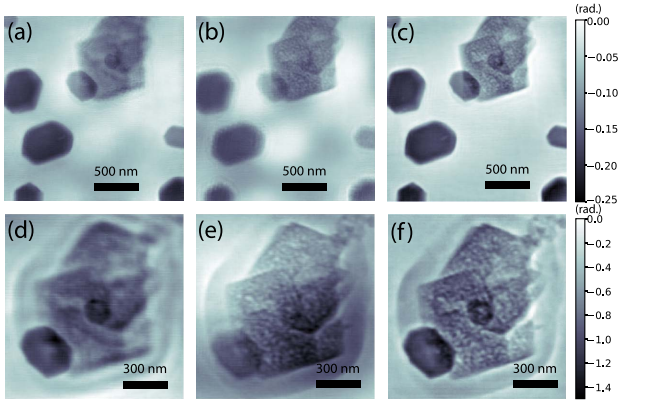


**Fig. 3.** Reconstructed phase images using the conventional and multi-slice ptychography. Top row and bottom row are the results from dataset 1 and dataset 2, respectively. (a)/(d) and (b)/(e) are the reconstructed images with conventional ptychography using the probe wavefronts at the front and rear surfaces, respectively. (c)/(f) Combined phase images with extended depth of field using two recovered planes from multi-slice ptychography reconstructions.

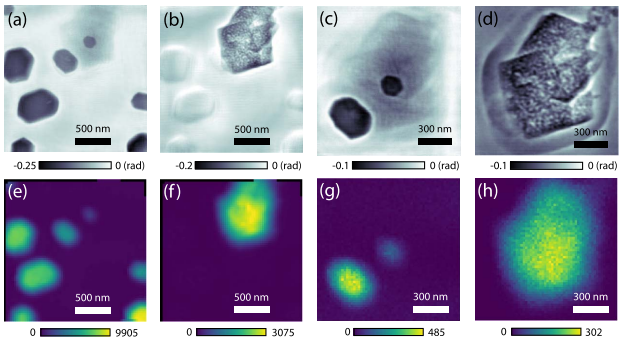


**Fig. 4.** Multi-slice ptychography and fluorescence images of the layered nanoparticles. (a)/(c) and (b)/(d) are the reconstructed phase images on the front and rear surfaces from dataset 1/dataset 2, respectively. (e)/(g) and (f)/(h) are the Au $L_\alpha$ and Ni $K_\alpha$ fluorescence maps for dataset 1/dataset 2. Fluorescence maps for dataset 1 were interpolated onto Cartesian coordinates. The measurements were conducted at a defocal plane, so that the fluorescence maps are blurry.

DoF of the obtained projection image is extended beyond the DoF of the optics.

Dataset 2 was collected in using the on-the-fly scheme with a Cartesian grid of scan points. A finer step size was used to suppress the periodic artifact [55]. Conventional reconstruction results with the probe functions at two planes are shown in Figs. 3(d) and 3(e), respectively. Five illumination modes were used in the reconstruction process to handle the partial coherent effect introduced by the continuous motion of the on-the-fly scan scheme [56]. At each plane, five illumination wavefronts interacted with the sample independently, while their final diffraction intensities were added together at the detector plane and updated with the measured intensity at each scan position. The illumination modes were initially calculated using conventional ptychographic reconstruction, and then were used as the initial probes and fixed in the first 50 iteration for the multi-slice reconstruction, which took 2000 iterations. The reconstructed illumination modes are shown in Supplement 1 Fig. S5. It is noticeable that since the multi-slice reconstruction includes additional propagation processes and recovers illumination and object functions on extra planes, it increases the computation time by a factor of 56 in our implementation. The calculation of five illumination modes adds another factor of 4.6. With the computation power provided by GPU accelerations [57–59], this increased calculation time is not expected to be a severe limitation in the practical applications.

We noticed that a drop-shaped mark was formed around the nickel oxide particle within the first few hours of x-ray exposure. The mark did not appear in the reconstruction of dataset 1. It started to show in a scan taken about 10 h later, and it is clearly visible in dataset 2 collected about another 10 h later. The mark is most likely a carbon layer, deposited under intense x-ray beam. The front surface of the sample was coated with a thin layer of chromium to improve the adhesion of the later deposited gold film to the silicon substrate. The electric conductivity of the front surface was significantly increased compared with the rear surface, so that the excited photoelectrons can be effectively conducted away, preventing the carbon deposition. This could explain why the carbon layer did not accumulate on the front surface. The reconstructed two slices are shown in Figs. 4(c) and 4(d), and the particle shapes and sizes agree very well with fluorescence maps [Figs. 4(g) and 4(h)]. Both particles are sharp in the combined projection image, as shown in Fig. 3(f).

To estimate the resolution of the reconstructed images, we compared the measured data with the diffraction pattern calculated from reconstructed probe and object images at different spatial frequencies. The phase retrieval transfer function (PRTF) is calculated [60] as $\mathrm{PRTF}(q) = \sum_i |\mathcal{F}\{P_i O_i\}(q)| / I_i(q)^{1/2}$, where $\mathcal{F}$ denotes the Fourier transform, $P$ and $O$ are the probe and object functions at the last plane, and the summation is over all scan positions. For dataset 2, the numerator is a summation over all five illumination modes with the object function on the last plane: $\{\sum_m |\mathcal{F}\{P_{i,m} O_i\}|^2\}^{1/2}$, $m = 1,2,\ldots,5$. The PRTF curve for dataset 1 remains above 0.8 to the highest spatial frequency used in the reconstruction (shown as the solid blue curve in Fig. 5). It implies that the phase information of all the cropped 128 × 128 pixels was faithfully reconstructed with 0.5 s dwell time, which suggests a lateral half-period resolution of 7.3 nm. For dataset 2 with 0.05 dwell time, the PRTF curve (shown as the solid orange curve in Fig. 5) starts to drop down when the spatial frequency goes beyond the holographic area boundary, which stands for a half-period of about 10.4 nm. Using the 0.5 threshold, the estimated lateral spatial resolution for dataset 2 is about 8.1 nm. The obtained resolution was confirmed with the Fourier shell correlation (FSC) method [61]. Shown in the inset of Fig. 5, the FSC of dataset 1 stays above the 1-bit threshold curve towards the spatial frequency determined by the array edge, while the intersection between the FSC of dataset 2 and the 1-bit threshold curve gives 9.2 nm resolution, which agrees well with the value obtained from the PRTF curve.

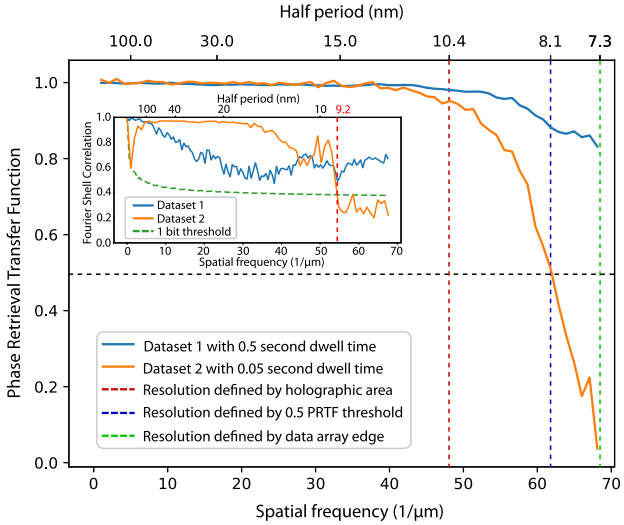


**Fig. 5.** Reconstruction resolution estimated by the phase retrieval transfer functions and the Fourier shell correlation. The PRTF shows that dataset 1 with 0.5 s dwell time was faithfully reconstructed to the edge of the cropped 128 × 128 data array, which corresponds to a half-period resolution of 7.3 nm. For dataset 2 with 0.05 s dwell time, the PRTF curve starts to fall down dramatically outside the holographic area, and the estimated resolution is about 8.1 nm using 0.5 threshold. The inset plots the FSC curves with the 1-bit threshold. The FSC curve of dataset 1 stays above the 1-bit threshold, while the intersection between the FSC of dataset 2 and the 1-bit threshold gives a 9.2 nm half-period resolution.

## 3. DISCUSSION

Our work demonstrates three major advantages of using high-NA MLLs for multi-slice ptychography: first, the narrower DoF naturally brings the axial sectioning capability down to the 4 μm level, which provides a moderate depth resolution; second, with the multiple scattering effect taken care of, the starting stage of the available lateral resolution defined by the point spread function of the lens is about 12 nm, from which the ptychography reconstruction can relatively easily push the resolution down to sub-10 nm level, which enables the capability to obtain high-resolution images from a thick specimen; third, using the intense holographic area diverged from the focused beam does not require a long dwell time to collect high-$q$ data, which significantly increases the throughput of this approach as a 3D imaging technique (a comparison with published works is shown in Supplement 1 Table 1). This method can be directly applied with high-NA zone plates [62,63] and KB mirrors [64,65].

The Rose criterion [66] states that a minimum SNR of 5 (i.e., intensity counts above 25) is required to distinguish image

features with sufficient certainty. A simulation study revealed that the image quality starts to deteriorate when the SNR is lower than 3 for the coherent diffraction imaging method [67], which suggests that the Rose criterion is applicable to the phase-retrieval based techniques. In our experiment, about 1300 photon counts were collected on average with 0.05 s dwell time in the holographic area. Applying the Rose criterion, the dwell time to fulfill the holographic area with sufficient SNR can be potentially reduced by another factor of 50 to 0.001 s level.

Extending the depth resolution beyond the DoF of optics requires collecting high-$q$ scattering signals outside the holographic area. A structured illumination with high-frequency profiles was proposed to assist spreading the scattering power into the high-$q$ range [68–70]. Adapting this idea to MLL optics, it might be beneficial to use imperfect MLLs for multi-slice ptychography applications. Zone placement errors can be purposely introduced in the MLL deposition process to add high-frequency structures in the focused probe, while retaining the same overall NA. Different zones could even be designed to have different focal lengths, thus forming a series of focal planes with DoF overlaps, which might be able to introduce redundancy along the axial direction. Another option is to use a diffuser, which is reported to facilitate the reconstruction especially for a sample with sparse features and areas with flat contrast [71]. The achievable NA can be extended beyond the detection limit using the superresolution mechanism [72], which has been demonstrated to extend the $q$ range by a factor of 3, with a structured illumination to increase the influence of high-$q$ signal.

For ptychography reconstructions, the limitation of lateral resolution $\delta r$ due to the sample thickness $T$ is suggested to be $T \leq 5.2(\delta r)^2/\lambda$ [7], which slightly differs from the DoF of optics $T \leq 4(\delta r)^2/\lambda$ [60]. Given the half-period resolution provided by the holographic area in this experiment is 10.4 nm, the thickness threshold for our setup is estimated to be 5.4 μm, which defines the DoF for each reconstructed plane. For a sample thickness above 5.4 μm, the multi-slice ptychography reconstruction can effectively improve the lateral resolution beyond the thickness limitation [27].

With the moderate depth resolution, the value of the multi-slice ptychography reconstruction is to obtain a high-resolution projection image with extended DoF. Combined with the tomography method, this capability is crucial for visualizing 3D structures of thick samples at high resolution.

## 4. CONCLUSION

In conclusion, we performed the multi-slice ptychography measurements using high-NA MLLs. Using the data inside the intense holographic region diverged from the nano-focused beam, a high lateral resolution (8.1 nm) and a moderate depth resolution (10 μm) were obtained with 0.05 s dwell time while imaging two layers of nanoparticles using the on-the-fly scan scheme. The 3D resolving power with extended DoF provided by the nano-focusing optics paves the way for multi-slice ptychography as a high-throughput technique for high-resolution 3D imaging of thick samples.

**Funding.** Office of Science (SC) (DE-SC0012704); Laboratory Directed Research and Development (LDRD) (LDRD-21690) program from the Brookhaven National Laboratory (BNL).

**Acknowledgment.** This research used resources of the National Synchrotron Light Source II, a U.S. Department of Energy (DOE) Office of Science User Facility operated for the DOE Office of Science by Brookhaven National Laboratory.

See Supplement 1 for supporting content.

## REFERENCES

1. D. Sayre, "Some implications of a theorem due to Shannon," Acta Crystallogr. **5**, 843 (1952).
2. J. Miao, P. Charalambous, J. Kirz, and D. Sayre, "An extension of the methods of x-ray crystallography to allow imaging of micron-size non-crystalline specimens," Nature **400**, 342–344 (1999).
3. J. Rodenburg, A. Hurst, A. Cullis, B. Dobson, F. Pfeiffer, O. Bunk, C. David, K. Jefimovs, and I. Johnson, "Hard-x-ray lensless imaging of extended objects," Phys. Rev. Lett. **98**, 034801 (2007).
4. F. Pfeiffer, "X-ray ptychography," Nat. Photonics **12**, 9–17 (2018).
5. Y. Takahashi, Y. Nishino, R. Tsutsumi, N. Zettsu, E. Matsubara, K. Yamauchi, and T. Ishikawa, "High-resolution projection image reconstruction of thick objects by hard x-ray diffraction microscopy," Phys. Rev. B **82**, 214102 (2010).
6. D. Shapiro, Y. Yu, T. Tyliszczak, J. Cabana, R. Celestre, W. Chao, K. Kaznatcheev, A. Kilcoyne, F. Maia, S. Marchesini, Y. Meng, T. Warwick, L. Yang, and H. Padmore, "Chemical composition mapping with nanometre resolution by soft x-ray microscopy," Nat. Photonics **8**, 765–769 (2014).
7. M. Holler, A. Diaz, M. Guizar-Sicairos, P. Karvinen, E. Farm, E. Harkonen, M. Ritala, A. Menzel, J. Raabe, and O. Bunk, "X-ray ptychographic computed tomography at 16 nm isotropic 3D resolution," Sci. Rep. **4**, 3857 (2014).
8. M. Holler, M. Guizar-Sicairos, E. Tsai, R. Dinapoli, E. Muller, O. Bunk, J. Raabe, and G. Aeppli, "High-resolution non-destructive three- dimensional imaging of integrated circuits," Nature **543**, 402–406 (2017).
9. C. Jacobsen, J. Deng, and Y. Nashed, "Strategies for high-throughput focused-beam ptychography," J. Synchrotron Radiat. **24**, 1078–1081 (2017).
10. H. Yan, J. Maser, A. Macrander, Q. Shen, S. Vogt, G. B. Stephenson, and H. Kang, "Takagi-Taupin description of x-ray dynamical diffraction from diffractive optics with large numerical aperture," Phys. Rev. B **76**, 115438 (2007).
11. H. Yan, R. Conley, N. Bouet, and Y. Chu, "Hard x-ray nanofocusing by multilayer Laue lenses," J. Phys. D: Appl. Phys. **47**, 263001 (2014).
12. H. Kang, J. Maser, G. B. Stephenson, C. Liu, R. Conley, A. T. Macrander, and S. Vogt, "Nanometer linear focusing of hard x rays by a multilayer Laue lens," Phys. Rev. Lett. **96**, 127401 (2006).
13. H. Kang, H. Yan, R. Winarski, M. Holt, J. Maser, C. Liu, R. Conley, S. Vogt, A. Macrander, and G. Stephenson, "Focusing of hard x-rays to 16 nanometers with a multilayer Laue lens," Appl. Phys. Lett. **92**, 221114 (2008).
14. H. Yan, V. Rose, D. Shu, E. Lima, H. Kang, R. Conley, C. Liu, N. Jahedi, A. Macrander, G. Stephenson, M. Holt, Y. Chu, M. Lu, and J. Maser, "Two dimensional hard x-ray nanofocusing with crossed multilayer Laue lenses," Opt. Express **19**, 15069–15076 (2011).
15. X. Huang, H. Yan, E. Nazaretski, R. Conley, N. Bouet, J. Zhou, K. Lauer, L. Li, D. Eom, D. Legnini, R. Harder, I. Robinson, and Y. Chu, "11 nm hard x-ray focus from a large-aperture multilayer Laue lens," Sci. Rep. **3**, 3562 (2013).
16. X. Huang, R. Conley, N. Bouet, J. Zhou, A. Macrander, J. Maser, H. Yan, E. Nazaretski, K. Lauer, R. Harder, I. Robinson, S. Kalbfleisch, and Y. Chu, "Achieving hard x-ray nanofocusing using a wedged multilayer Laue lens," Opt. Express **23**, 12496–12507 (2015).
17. A. Morgan, M. Prasciolu, A. Andrejczuk, J. Krzywinski, A. Meents, D. Pennicard, H. Graafsma, A. Barty, R. Bean, M. Barthelmess, D. Oberthuer, O. Yefanov, A. Aquila, H. Chapman, and S. Bajt, "High numerical aperture multilayer Laue lenses," Sci. Rep. **5**, 9892 (2015).
18. X. Huang, W. Xu, E. Nazaretski, N. Bouet, J. Zhou, Y. Chu, and H. Yan, "Hard x-ray scanning imaging achieved with bonded multilayer Laue lenses," Opt. Express **25**, 8698–8704 (2017).
19. S. Bajt, M. Prasciolu, H. Fleckenstein, M. Domaracký, H. Chapman, A. Morgan, O. Yefanov, M. Messerschmidt, Y. Du, K. Murray,

V. Mariani, M. Kuhn, S. Aplin, K. Pande, P. Villanueva-Perez, K. Stachnik, J. Chen, A. Andrejczuk, A. Meents, A. Burkhardt, D. Pennicard, X. Huang, H. Yan, E. Nazaretski, Y. Chu, and C. Hamm, "X-ray focusing with efficient high-NA multilayer Laue lenses," Light: Sci. Appl. **7**, 17162 (2018).
20. M. Jones, K. Elgass, M. Junker, M. Luu, M. Ryan, A. Peele, and G. van Riessen, "Mapping biological composition through quantitative phase and absorption x-ray ptychography," Sci. Rep. **5**, 9892 (2015).
21. J. Deng, D. Vine, S. Chen, Y. Nashed, Q. Jin, N. Phillips, T. Peterka, R. Ross, S. Vogt, and C. Jacobsen, "Simultaneous cryo x-ray ptychography and fluorescence microscopy of green algae," Proc. Natl. Acad. Sci. USA **112**, 2314–2319 (2015).
22. J. Deng, D. Vine, S. Chen, Q. Jin, Y. Nashed, T. Peterka, S. Vogt, and C. Jacobsen, "X-ray ptychographic and fluorescence microscopy of frozen-hydrated cells using continuous scanning," Sci. Rep. **7**, 445 (2017).
23. J. Clark, X. Huang, R. Harder, and I. Robinson, "Continuous scanning mode for ptychography," Opt. Lett. **39**, 6066–6069 (2014).
24. P. Pelz, M. Guizar-Sicairos, P. Thibault, I. Johnson, M. Holler, and A. Menzel, "On-the-fly scans for x-ray ptychography," Appl. Phys. Lett. **105**, 251101 (2014).
25. X. Huang, K. Lauer, J. Clark, W. Xu, E. Nazaretski, R. Harder, I. Robinson, and Y. Chu, "Fly-scan ptychography," Sci. Rep. **5**, 9074 (2015).
26. J. Deng, Y. Nashed, S. Chen, N. Phillips, T. Peterka, R. Ross, S. Vogt, C. Jacobsen, and D. Vine, "Continuous motion scan ptychography: characterization for increased speed in coherent x-ray imaging," Opt. Express **23**, 5438–5451 (2015).
27. E. Tsai, I. Usov, A. Diaz, A. Menzel, and M. Guizar-Sicairos, "X-ray ptychography with extended depth of field," Opt. Express **24**, 29089–29108 (2016).
28. J. Cowley and A. Moodie, "The scattering of electrons by atoms and crystals. I. A new theoretical approach," Acta Crystallogr. **10**, 609–619 (1957).
29. P. Goodman and A. Moodie, "Numerical evaluations of N-beam wave functions in electron scattering by the multi-slice method," Acta Crystallogr. **A30**, 280–290 (1974).
30. A. Maiden, M. Humphry, and J. Rodenburg, "Ptychographic transmission microscopy in three dimensions using a multi-slice approach," J. Opt. Soc. Am. A **29**, 1606–1614 (2012).
31. T. Godden, R. Suman, M. Humphry, J. Rodenburg, and A. Maiden, "Ptychographic microscope for three-dimensional imaging," Opt. Express **22**, 12513–12523 (2014).
32. S. Gao, P. Wang, F. Zhang, G. Martinez, P. Nellist, X. Pan, and A. Kirkland, "Electron ptychographic microscopy for three-dimensional imaging," Nat. Commun. **8**, 163 (2017).
33. G. Zheng, R. Horstmeyer, and C. Yang, "Wide-field, high-resolution Fourier ptychographic microscopy," Nat. Photonics **7**, 739–745 (2013).
34. P. Li, D. Batey, T. Edo, and J. Rodenburg, "Separation of three-dimensional scattering effects in tilt-series Fourier ptychography," Ultramicroscopy **158**, 1–7 (2015).
35. L. Tian and L. Waller, "3D intensity and phase imaging from light field measurements in an LED array microscope," Optica **2**, 104–111 (2015).
36. Q. Shen, I. Bazarov, and P. Thibault, "Diffractive imaging of nonperiodic materials with future coherent x-ray sources," J. Synchrotron Radiat. **11**, 432–438 (2004).
37. A. Suzuki, S. Furutaku, K. Shimomura, K. Yamauchi, Y. Kohmura, T. Ishikawa, and Y. Takahashi, "High-resolution multislice x-ray ptychography of extended thick objects," Phys. Rev. Lett. **112**, 053903 (2014).
38. K. Shimomura, A. Suzuki, M. Hirose, and Y. Takahashi, "Precession x-ray ptychography with multislice approach," Phys. Rev. B **91**, 214114 (2015).
39. K. Shimomura, M. Hirose, and Y. Takahashi, "Multislice imaging of integrated circuits by precession x-ray ptychography," Acta Crystallogr. Sec. A **74**, 66–70 (2018).
40. G. Williams, H. Quiney, B. Dhal, C. Tran, K. Nugent, A. Peele, D. Paterson, and M. de Jonge, "Fresnel coherent diffractive imaging," Phys. Rev. Lett. **97**, 025506 (2006).
41. E. Nazaretski, K. Lauer, H. Yan, N. Bouet, J. Zhou, R. Conley, X. Huang, W. Xu, M. Lu, K. Gofron, S. Kalbfleisch, U. Wagner, C. Rau, and Y. Chu, "Pushing the limits: an instrument for hard x-ray imaging below 20 nm," J. Synchrotron Radiat. **22**, 336–341 (2015).
42. E. Nazaretski, H. Yan, K. Lauer, N. Bouet, X. Huang, W. Xu, J. Zhou, D. Shu, Y. Hwu, and Y. Chu, "Design and performance of an x-ray scanning microscope at the Hard X-ray Nanoprobe beamline of NSLS-II," J. Synchrotron Radiat. **24**, 1113–1119 (2017).
43. H. Yan, E. Nazaretski, K. Lauer, X. Huang, U. Wagner, C. Rau, M. Yusuf, I. Robinson, S. Kalbfleisch, L. Li, N. Bouet, J. Zhou, R. Conley, and Y. Chu, "Multimodality hard-x-ray imaging of a chromosome with nanoscale spatial resolution," Sci. Rep. **6**, 20112 (2016).
44. H. Feng, Y. Qian, J. Cochran, Q. Zhu, W. Hu, H. Yan, L. Li, X. Huang, Y. Chu, H. Liu, S. Yoo, and C. Liu, "Nanoscale measurement of trace element distributions in Spartina alterni ora root tissue during dormancy," Sci. Rep. **7**, 40420 (2017).
45. H. Yan, J. Maser, H. Kang, A. Macrander, and G. Stephenson, "A theoretical study of two-dimensional point focusing by two multilayer Laue lenses," Proc. SPIE **7077**, 70770Q (2008).
46. H. Yan, X. Huang, N. Bouet, J. Zhou, E. Nazaretski, and Y. Chu, "Achieving diffraction-limited nanometer-scale x-ray point focus with two crossed multilayer Laue lenses: alignment challenges," Opt. Express **25**, 25234–25242 (2017).
47. R. Plackett, I. Horswell, E. Gimenez, J. Marchal, D. Omar, and N. Tartoni, "Merlin: a fast versatile readout system for Medipix3," J. Instrum. **8**, C01038 (2013).
48. O. Bunk, M. Dierolf, S. Kynde, I. Johnson, O. Marti, and F. Pfeiffer, "Influence of the overlap parameter on the convergence of the ptychographical iterative engine," Ultramicroscopy **108**, 481–487 (2008).
49. X. Huang, H. Yan, R. Harder, Y. Hwu, I. Robinson, and Y. Chu, "Optimization of overlap uniformness for ptychography," Opt. Express **22**, 12634–12644 (2014).
50. P. Thibault, M. Dierolf, A. Menzel, O. Bunk, C. David, and F. Pfeiffer, "High-resolution scanning x-ray diffraction microscopy," Science **321**, 379–382 (2008).
51. J. Spence, U. Weierstall, and M. Howells, "Phase recovery and lensless imaging by iterative methods in optical, x-ray and electron diffraction," Philos. Trans. R. Soc. London **360**, 875–895 (2002).
52. X. Huang, R. Harder, G. Xiong, X. Shi, and I. Robinson, "Propagation uniqueness in three-dimensional coherent diffractive imaging," Phys. Rev. B **83**, 224109 (2011).
53. I. Robinson and X. Huang, "Reaching the third dimension," Nat. Mater. **16**, 160–161 (2017).
54. B. Frieden, "Optical transfer of the three-dimensional object," J. Opt. Soc. Am. **57**, 56–66 (1967).
55. X. Huang, H. Yan, M. Ge, H. Ozturk, E. Nazaretski, I. Robinson, and Y. Chu, "Artifact mitigation of ptychography integrated with on-the-fly scanning probe microscopy," Appl. Phys. Lett. **111**, 023103 (2017).
56. P. Thibault and A. Menzel, "Reconstructing state mixtures from diffraction measurements," Nature **494**, 68–71 (2013).
57. Y. Nashed, D. Vine, T. Peterka, J. Deng, R. Ross, and C. Jacobsen, "Parallel ptychographic reconstruction," Opt. Express **22**, 32082–32097 (2014).
58. S. Marchesini, H. Krishnan, B. Daurer, D. Shapiro, T. Perciano, J. Sethiana, and F. Maiab, "SHARP: a distributed GPU-based ptychographic solver," J. Appl. Crystallogr. **49**, 1245–1252 (2016).
59. B. Enders and P. Thibault, "A computational framework for ptychographic reconstructions," Proc. R. Soc. London Ser. A **472**, 20160640 (2016).
60. H. Chapman, A. Barty, S. Marchesini, A. Noy, S. Hau-Riege, C. Cui, M. Howells, R. Rosen, H. He, J. Spence, U. Weierstall, T. Beetz, C. Jacobsen, and D. Shapiro, "High-resolution ab initio three-dimensional x-ray diffraction microscopy," J. Opt. Soc. Am. A **23**, 1179–1200 (2006).
61. M. van Heel and M. Schatz, "Fourier shell correlation threshold criteria," J. Struct. Biol. **151**, 250–262 (2005).
62. K. Jefimovs, J. Vila-Comamala, T. Pilvi, J. Raabe, M. Ritala, and C. David, "Zone-doubling technique to produce ultrahigh-resolution x-ray optics," Phys. Rev. Lett. **99**, 264801 (2007).
63. W. Chao, J. Kim, S. Rekawa, P. Fischer, and E. Anderson, "Demonstration of 12 nm resolution Fresnel zone plate lens based soft x-ray microscopy," Opt. Express **17**, 17669–17677 (2009).
64. H. Mimura, S. Handa, T. Kimura, H. Yumoto, D. Yamakawa, H. Yokoyama, S. Matsuyama, K. Inagaki, K. Yamamura, Y. Sano, K. Tamasaku, Y. Nishino, M. Yabashi, T. Ishikawa, and K. Yamauchi, "Breaking the 10 nm barrier in hard-x-ray focusing," Nat. Phys. **6**, 122–125 (2010).
65. J. D. Silva, A. Pacureanu, Y. Yang, S. Bohic, C. Morawe, R. Barrett, and P. Cloetens, "Efficient concentration of high-energy x-rays for diffraction-limited imaging resolution," Optica **4**, 492–495 (2017).

66. A. Rose, *Vision—Human and Electronic* (Plenum, 1973).
67. J. Miao, T. Ohsuna, O. Terasaki, K. Hodgson, and M. O'Keefe, "Atomic resolution three-dimensional electron diffraction microscopy," Phys. Rev. Lett. **89**, 155502 (2002).
68. A. Maiden, J. Rodenburg, and M. Humphry, "Optical ptychography: a practical implementation with useful resolution," Opt. Lett. **35**, 2585–2587 (2010).
69. M. Guizar-Sicairos, M. Holler, A. Diaz, J. Vila-Comamala, O. Bunk, and A. Menzel, "Role of the illumination spatial-frequency spectrum for ptychography," Phys. Rev. B **86**, 100103 (2012).
70. A. Maiden, G. Morrison, B. Kaulich, A. Gianoncelli, and J. Rodenburg, "Soft x-ray spectromicroscopy using ptychography with randomly phased illumination," Nat. Commun. **4**, 1669 (2013).
71. P. Li, D. Batey, T. Edo, A. Parsons, C. Rau, and J. Rodenburg, "Multiple mode x-ray ptychography using a lens and a fixed diffuser optic," J. Opt. **18**, 054008 (2016).
72. A. Maiden, M. Humphry, F. Zhang, and J. Rodenburg, "Superresolution imaging via ptychography," J. Opt. Soc. Am. A **28**, 604–612 (2011).